Hindawi
International Transactions on Electrical Energy Systems
Volume 2022, Article ID 4362886, 22 pages
https://doi.org/10.1155/2022/4362886

Research Article

Design and Development of Fixed-Frequency Double-Integral SM-Controlled Solar-Integrated Bidirectional Quasi *Z*-Source DC-DC Converter in Standalone Battery Connected System

Santhoshkumar Battula,[1] **Anup Kumar Panda**,[1] **and Man Mohan Garg**[2]

[1]*National Institute of Technology Rourkela, Rourkela, India*
[2]*Malaviya National Institute of Technology Jaipur, Jaipur, India*

Correspondence should be addressed to Man Mohan Garg; mmgarg.ee@mnit.ac.in

Received 17 December 2021; Revised 16 April 2022; Accepted 18 May 2022; Published 8 August 2022

Academic Editor: Qiuye Sun

DC microgrids have been quite popular in recent times. The operational challenges like control and energy management of the renewable-driven standalone DC microgrids have been an interest of research. This paper presents a bidirectional quasi *Z*-source DC-DC converter (BQZSDC). This converter topology has been developed based on a conventional buck-boost type bidirectional converter, and it interfaces the storage system and the common DC bus. The challenge, however, lies in effectively managing the uncertain renewable energy sources and the storage system and catering for the loads simultaneously. An effective control strategy is needed for that energy management and to achieve various microgrid objectives. This paper deals with one such effective control strategy implemented for BQZSDC. That is, the fixed-frequency double-integral sliding mode control (FF-DISMC) controls the converter to regulate the DC bus voltage and battery current. A detailed analysis of the controller is conducted, and its performance is evaluated for both charging (buck) and discharging (boost) modes. Simulations have been performed in MATLAB, showing that the controller performs satisfactorily in achieving the objectives of voltage regulation and battery current regulation. Finally, the performance of the proposed controller is validated with the hardware setup.

1. Introduction

Often, in applications requiring increased voltage, a conventional boost converter is a common choice. However, it is understood that voltage boosting is limited by duty cycle constraints because of the switching device performance and conduction loss [1–3]. Therefore, topologies with higher voltage gain have been of great research interest. In this line, the *Z*-source network's novel and effective topology came into the limelight [4]. The initial implementation of this topology was limited to DC-AC application, where the topology was popularly known as *Z*-source inverter (ZSI). This converter also supports bidirectional operation with both buck and boost modes. A significant amount of literature has been devoted to the ZSI and its applications, such as interfacing renewable sources like PV wind [5–7]. An improved version of the inverter named quasi *Z*-Source inverter (QZSI), with added advantages of input current continuity and reduced voltage stresses of capacitors, was introduced [8].

For DC-DC applications, the concepts of *Z*-source converter and quasi *Z*-source converter (QZSC) are often used [9–11]. In [12], QZSC has been used in bidirectional power flow applications, where the buck and boost modes were individually controlled [13, 14]. However, in the case of the converter connected to a standalone microgrid, it is essential that the DC link voltage is regulated in both modes of operation based on the power demand [14–17].

The *Z*-source and quasi-*Z*-source converters have simple architectures, and they can provide a significant gain [12].

The switched-inductor DC-DC converter proposed in [18] has high gain and low voltage stress, but it has more inductors. Reference [19] proposes a switched-capacitor-based *Z*-source DC-DC converter. In this topology, despite increased voltage gain, there is no common ground between input and output and it has high voltage stress across the switches. The switched-capacitor quasi *Z*-source DC-DC converter proposed in [20] has high efficiency, but more switches are required. The bidirectional quasi *Z*-source converter proposed in [21] can provide high gain but does not have common ground. This produces a *du/dt* issue between input and output.

The proposed BQZSDC can provide high voltage gain. Its design is based on the bidirectional quasi *Z*-source DC-DC two-level converter. The main difference is changing the primary power switch to a different position. This BQZSDC has minimal voltage stress on power switches. Consequently, the BQZSDC can choose power switches with low rated voltage and low on-state resistance, which causes improvement in efficiency. At the same time, when compared with basic quasi *Z*-source, its gain has been decreased slightly, but it still meets the requirements of connection with different sources. The presence of common ground also avoids the *du/dt* issue.

The conventional proportional-integral (PI) and dual-loop PI-control techniques are commonly designed by linearizing the model at a particular operating point [22, 23]. For higher-order systems, deriving a linearized model is complex. A reduced-order small-signal closed-loop transfer function model was presented in [24]. In this paper, traditional model order reduction procedures are utilized, and the inaccuracy of input-output mappings between the original and reduced-order systems is considerable. Wang et al. [25] propose to give a preprocessing strategy for real-time modeling of large-scale converters with inhomogeneous initial conditions to address input-output mapping problems. However, the transient behavior of these systems with linear controllers is poor under large-signal perturbations. This is because of the variaiton in small-signal models at different dc operting points. Several nonlinear controllers are utilized for power electronic converters to solve the above problems.

Sliding mode control (SMC) is a robust control approach that effectively handles parameter changes, external disturbances, and input disturbances. The hysteresis modulating sliding mode control (HM-SMC) technique used in [26–28] suffers from chattering and switching frequency variation under load fluctuations. In variable frequency operation, stabilizing the feedback control circuit could be difficult. Later, fixed-frequency SMC was developed using pulse width modulation [29], maintaining the constant frequency despite input voltage and load variations. This fixed-frequency SMC was based on an equivalent control switching function to harvest a trajectory near equivalent to an ideal sliding mode trajectory. SMC in conjunction with PWM reduces steady-state error (SSE) significantly. Integral SMC, which incorporates an integral term of the state variables into the SM controller, can further minimize SSE. A second integral component of the tracking error has been considered to improve the system's steady-state accuracy even more. Double-integral sliding mode controller (DISMC) responds quickly for a broader range of operating circumstances while significantly reducing SSE [30].

The model predictive control (MPC) computes the switch input from the converter's active model and provides a resolution for trajectory optimization [31]. The optimization techniques in MPC necessitate many computations, and MPC is not appropriately aimed at converters with large values of switching frequencies. References [32, 33] proposed voltage source inverters based on adaptive error correction, with the error approach included in both the outer and inner prediction loops and a nonlinear state-space function to describe the AC microgrid along with an event-triggered consensus control technique. However, MPC requires a powerful processor to perform real-time calculations, but DISMC has very simple calculations. The advantage of the proposed FF-DISMC is its ability to reject disturbances and deal with system uncertainties better than MPC.

The advantages of the proposed fixed-frequency double-integral SMC are as follows:

(1) Fast dynamic responses compared with conventional voltage and current mode controllers

(2) Characteristic robust features of SMC, but working at a fixed frequency

(3) Stability over a wider range of operating conditions

(4) The slight variation of the settling time over an extensive range of operating conditions

(5) Stabilizing the feedback control circuit can be more difficult in variable frequency operation than fixed-frequency control

The key contribution of this paper is the design and implementation of an FF-DISMC for the BQZSDC. The controller scheme was designed to regulate the DC grid voltage against variations in reference voltage and load power with bidirectional power flow.

Figure 1 depicts the proposed system's architecture. The suggested converter simultaneously manages the PV system's power, battery, and load. When solar radiation is available, a maximum power point tracking (MPPT) algorithm ensures that the PV panel generates the most power possible. The suggested controller directs the battery to absorb excess energy from the PV panel or supply the load with the power it requires.

Section 2 presents the system design and steady-state mathematical model of BQZSDC. The control strategy of FF-DISMC is analyzed in Section 3. The simulation and hardware results are shown in Section 4, comparison analysis in Section 5, and conclusions in Section 6.

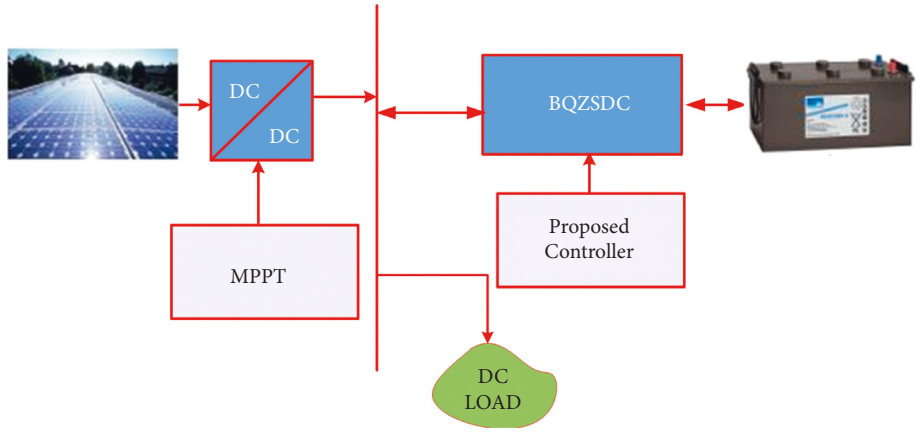

Figure 1: The architecture of the proposed standalone system.

2. System Design and Modeling

The following assumptions are made in the proposed BQZSDC to simplify the analysis:

(1) The power switches' on-state resistance and the equivalent series resistance of the inductors L_1, L_2 and capacitors C_1, C_0 are Ignored. The ESR, r of capacitor C_2, is considered to avoid complications in obtaining the state equations of the converter.

(2) The currents and voltages of the inductors and capacitors increase and decrease linearly.

(3) The voltage across the battery was constant.

The topology of the BQZSDC is displayed in Figure 2, interfacing the battery storage to the load and DC bus. The topology primarily consists of three active switches, S_1, S_2, and S_3. The converter has the bidirectional capability to charge/discharge the battery by adequately choosing the switching signals. In this paper, the operation of the converter in boost mode (discharging mode) is only analyzed; however, buck mode can also be operated similarly. In the boost mode of the converter, the switch S_1 acts as the main switch, whereas S_2 and S_3 are complementary switches to S_1. The battery voltage V_b is assumed to be constant.

It is considered that BQZSDC is being operated in CCM, with switching input u and a constant switching frequency f. The converter operation can best be analyzed by observing the following two modes individually.

2.1. Mode 1: S_1 Is Turned On; S_2 and S_3 Are Turned Off ($0 < t \le DT$). In mode 1, S_1 is made on and switches S_2 and S_3 are made off. Once the switching status of the switches S_1, S_2, and S_3 is declared, the topology can be seen in Figure 3. On analyzing the circuit, it can be understood that the energy from the battery is stored in the inductor L_1 with S_1 being turned on. The capacitor C_2 gets energized through L_2 and C_1 (already charged). The load power in this mode is supplied by the output capacitor C_0 because the load is straight away not attached to the battery.

The switching states in this mode are as follows:

$$v_{L1} = L_1 \frac{di_{L1}}{dt} = v_b, \tag{1}$$

$$v_{L2} = L_2 \frac{di_{L2}}{dt} = v_{C1} - v_{C2} - i_{L2} r, \tag{2}$$

$$i_{C1} = C_1 \frac{dv_{C1}}{dt} = -i_{L2}, \tag{3}$$

$$i_{C2} = C_2 \frac{dv_{C2}}{dt} = i_{L2}, \tag{4}$$

$$i_{C0} = C_0 \frac{dv_0}{dt} = -\frac{v_0}{R_0} = -i_{\text{Load}}. \tag{5}$$

2.2. Mode 2: S_1 Is Turned Off; S_2 and S_3 Are Turned On ($DT < t \le T$). In mode 2, S_1 is turned off and switches S_2 and S_3 are turned on. The topology can be seen as the equivalent circuit in Figure 4. As a consequence of the previous mode, the energy kept in the inductor L_1 charges the capacitor C_1 through S_2. The energy kept in the inductor L_2 is used to feed the load R_0, and the capacitor C_2 is discharged simultaneously.

The switching states in this mode are as follows:

$$v_{L1} = L_1 \frac{di_{L1}}{dt} = v_b - v_{C1}, \tag{6}$$

$$v_{L2} = L_2 \frac{di_{L2}}{dt} = v_{C1} - v_0, \tag{7}$$

$$i_{C1} = C_1 \frac{dv_{C1}}{dt} = i_{L1} - i_{L2} + \frac{v_0 - v_{C1} - v_{C2}}{r}, \tag{8}$$

$$i_{C2} = C_2 \frac{dv_{C2}}{dt} = \frac{v_0 - v_{C1} - v_{C2}}{r}, \tag{9}$$

$$i_{C0} = C_0 \frac{dv_0}{dt} = i_{L2} - \frac{v_0 - v_{C1} - v_{C2}}{r} - \frac{v_0}{R_0}. \tag{10}$$

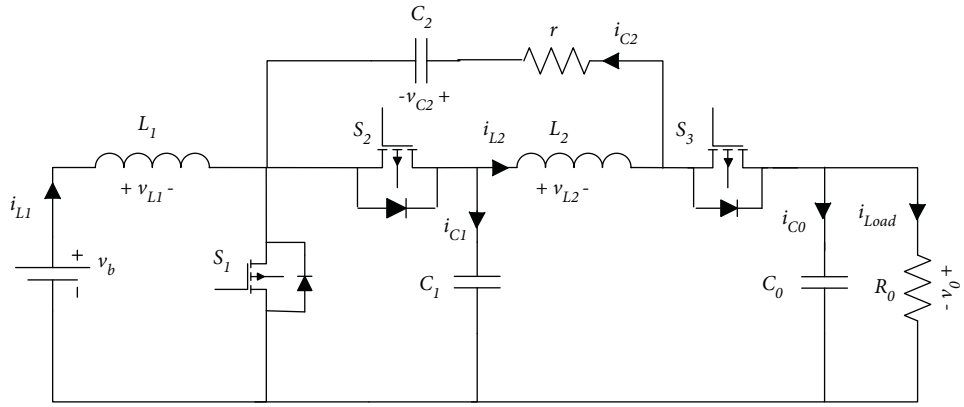

Figure 2: Circuit diagram of BQZSDC.

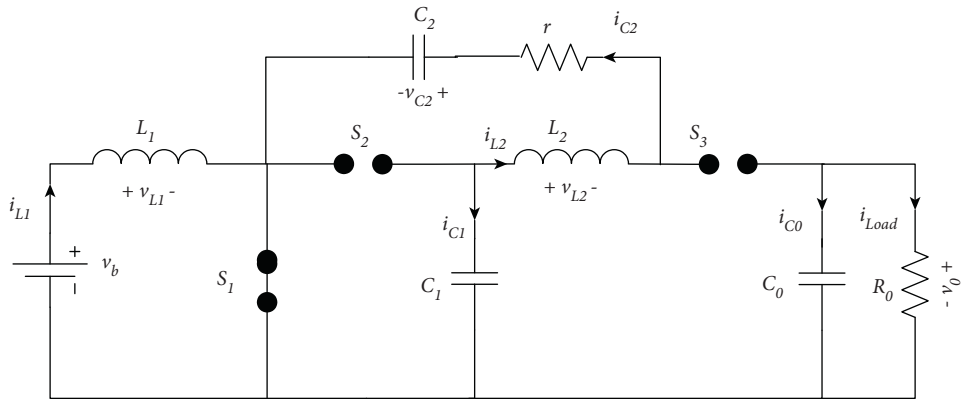

Figure 3: BQZSDC in mode 1 ($0 < t \leq \mathrm{DT}$).

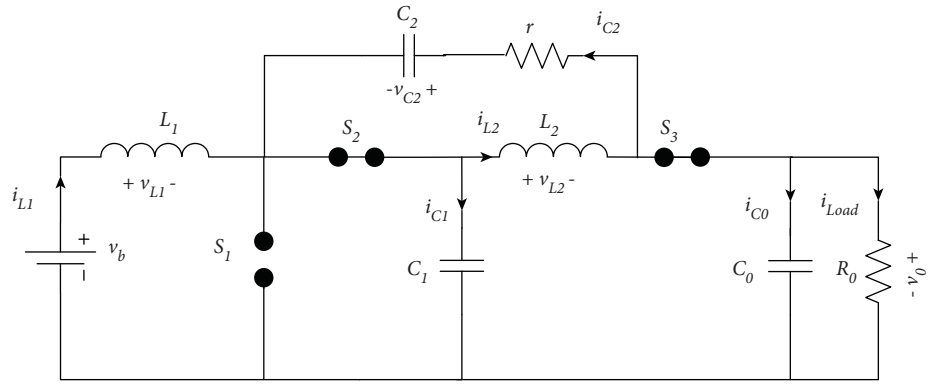

Figure 4: BQZSDC in mode 2 ($\mathrm{DT} < t \leq T$).

2.2.1. State-Model Representation. With (1) to (10), we derive the system modeled as follows:

$$\dot{X} = A + Bu, \tag{11}$$

where u indicates the switching state of S_1 and matrices A and B are as follows:

$$A = \begin{bmatrix} \frac{1}{L_1}(v_b - v_{C1}) \\ \frac{1}{L_2}(v_{C1} - v_0) \\ \frac{1}{C_1}(i_{L1} - i_{L2}) + \frac{1}{C_1 r}(v_0 - v_{C1} - v_{C2}) \\ \frac{1}{C_2 r}(v_0 - v_{C1} - v_{C2}) \\ \frac{1}{C_0}\left(\frac{-v_0}{R_0}\right) + \frac{i_{L2}}{C_0} - \frac{1}{C_0 r}(v_{C_0} - v_{C1} - v_{C2}) \end{bmatrix},$$

$$B = \begin{bmatrix} \frac{v_{C1}}{L_1} \\ \frac{1}{L_2}(v_0 - v_{C2} - i_{L2} r) \\ \frac{-i_{L1}}{C_1} - \frac{1}{C_1 r}(v_0 - v_{C1} - v_{C2}) \\ \frac{i_{L2}}{C_2} - \frac{1}{C_2 r}(v_0 - v_{C1} - v_{C2}) \\ -\frac{i_{L2}}{C_0} + \frac{1}{C_0 r}(v_0 - v_{C1} - v_{C2}) \end{bmatrix}. \tag{12}$$

The state vector includes five parameters: inductor currents i_{L1} and i_{L2} and capacitor voltages v_{C1}, v_{C2}, and v_0.

The state vector is presented as follows:

$$X = [\, i_{L1} \;\; i_{L2} \;\; v_{C1} \;\; v_{C2} \;\; v_0 \,]^T. \tag{13}$$

3. Fixed-Frequency Double-Integral Sliding Mode Control

The proposed FF-DISMC has two significant features. This controller is based on reduced state measures operating at a fixed frequency [29]. The advantage of fixed frequency operation is explained in Section 1. The output voltage measured and the remaining state variables are estimated to sense the minimum number of state variables. Here, the controller variables are errors in output voltage (v_0) and input current (i_{L1}). The reference current (i_{ref}) for inductor L_1 is generated using voltage error:

$$i_{\text{ref}} = K(v_{\text{ref}} - v_0). \tag{14}$$

3.1. Sliding Surface. The proposed FF-DISM control employs the output voltage (v_0) and battery side inductor current (i_{L1}) errors as control state variables. Correspondingly, two more control state variables are added to the sum of the first two state variables as integrals and double integrals.

The control variables are further shown as follows:

$$x_1 = i_{L_{1\text{ref}}} - i_{L1}, \tag{15}$$

$$x_2 = v_{\text{ref}} - v_0, \tag{16}$$

$$x_3 = \int (x_1 + x_2)\mathrm{d}t, \tag{17}$$

$$x_4 = \int\int (x_1 + x_2)\mathrm{d}t. \tag{18}$$

For the control of BQZSDC, the switch input u should limit values between 0 and 1.

$$u = \begin{cases} 1, & s > 0, \\ 0, & s < 0. \end{cases} \tag{19}$$

This control logic is developed by expressing the logic state of S_1. The switching function is as follows:

$$u = \frac{1}{2}(1 + \operatorname{sign}(\dot{s})). \tag{20}$$

The FF-DISM controller's sliding surfaces are most likely to be interpreted as a linear combination of four state variables, which can be expressed as follows:

$$s = \alpha_1 x_1 + \alpha_2 x_2 + \alpha_3 x_3 + \alpha_4 x_4, \tag{21}$$

where α_1, α_2, α_3, and α_4 are the sliding coefficients.

3.2. Equivalent Control. The dynamic model of the BQZSDC can be obtained by substituting a set of equations in (11) into the time derivative converter variables given in (15)–(18). The derived equations are shown as follows:

$$\begin{aligned} \dot{x}_1 &= -K\frac{i_{C_0}}{C_0} - \frac{1}{L_1}(V_b - v_{C1}(1-u)), \\ \dot{x}_2 &= \frac{-i_{C_0}}{C_0}, \\ \dot{x}_3 &= \frac{i_{C_0}}{C_0}(K+1) - \frac{1}{L_1}(v_b - v_{C1}(1-u)), \\ \dot{x}_4 &= \int (x_1 + x_2)\mathrm{d}t. \end{aligned} \tag{22}$$

The equivalent control equation was derived by implementing equation $\dot{s} = 0$.

This gives the following:

$$u_{eq} = \frac{1}{v_{C1}}\left(-L_1\frac{i_{C0}}{C_0}\left(K+\frac{\alpha_2}{\alpha_1}\right) - v_b + v_{C1} + \frac{\alpha_3 L_1}{\alpha_1}(x_1+x_2)\right) + \frac{1}{v_{C1}}\left(\frac{\alpha_4 L_1}{\alpha_1}\left(\int (x_1+x_2)\mathrm{d}t\right)\right). \tag{23}$$

3.3. The Architecture of the Proposed Controller. A PWM block and a group of control rules, which were based on indirect SM control, are used to implement the proposed FF-DISM controller [34,35]. The equivalent controller consists of a control signal $v_C$and a ramp signal v_{ramp} as follows:

$$v_C = \left(-i_{C_0}k_3 - v_b + v_{C1} + k_1(x_1+x_2) + k_2\left(\int (x_1+x_2)\mathrm{d}t\right)\right),$$
$$v_{\text{ramp}} = v_{C_1}, \tag{24}$$

where

$$k_1 = L_1\frac{\alpha_3}{\alpha_1},$$
$$k_2 = L_1\frac{\alpha_4}{\alpha_1}, \tag{25}$$
$$k_3 = \frac{L_1}{C_0}\left(K+\frac{\alpha_2}{\alpha_1}\right).$$

The BQZSDC and the FF-DISM controller are shown in Figure 5. The control law includes the comparison of the two signals v_C and v_{ramp}. The ramp signal maintains the constant frequency.

For successful sliding mode operation, it is essential to satisfy three conditions. These conditions are hitting conditions, existing conditions, and stability conditions. The hitting condition confirms that the state trajectory hits the sliding surface, which was guaranteed by the switching function used in (20).

3.4. Existence Conditions. To examine the existence condition, it must satisfy the local reachability conditions given as follows:

$$\lim_{s\longrightarrow 0} s\dot{s} > 0. \tag{26}$$

Replacing the derivative of (21) in (26), we can state the equation as follows:

$$\dot{s}_{s\longrightarrow 0^+} > 0, \tag{27}$$

$$\dot{s}_{s\longrightarrow 0^-} > 0. \tag{28}$$

For BQZSDC, the existence conditions for the sliding mode operation are as follows:

In the case-1, $s \longrightarrow 0^+$, $\dot{s} < 0$.

Substituting $u_{s\longrightarrow 0^+} = 1$ into (27), we have the following:

$$k_1(x_1+x_2) - v_b - i_{C0}k_3 + k_2x_3 < 0. \tag{29}$$

In the case-2, $s \longrightarrow 0^-$, $\dot{s} > 0$.

Substituting $u_{s\longrightarrow 0^-} = 1$ into (28), we have the following:

$$k_1(x_1+x_2) - v_b + v_{C1} - i_{C0}k_3 + k_2x_3 > 0. \tag{30}$$

The values of battery voltage V_b and output voltage V_0 are assumed within a limit, which typically depict an operating range of the converter. The existing condition at maximum and minimum values is sufficient to ensure the broad range of abidance. While designing a sliding mode controller, the existing conditions should be met for steady-state operation. At steady-state condition, the state variables v_{C1}, v_{C2} in (29), (30) are replaced by steady-state values V_{C1} (SS), V_{C2} (SS).

Equations (31) and (32) can show the resulting existing condition considering all presumptions:

$$k_1x_1 + k_1\left(v_{\text{ref}} - v_{o(\min)}\right) - v_{b(\min)} - i_{C0}k_3 + k_2\int x_1\mathrm{d}t + k_2\int\left(v_{\text{oref}} - v_{o(\min)}\right) < 0, \tag{31}$$

$$k_1x_1 + k_1\left(v_{o(\text{ref})} - v_{o(\max)}\right) - v_{b(\max)} + v_{C1} - i_{C0}k_3 + k_2\int x_1\mathrm{d}t + k_2\int v_{o(\text{ref})} - v_{o(\max)} > 0. \tag{32}$$

3.5. Stability Condition. The stability condition for the controller was proved by first determining the system's ideal sliding dynamics and then analyzing its equilibrium point.

3.5.1. Ideal Sliding Dynamics. By substituting u by u_{eq} in (11), the large-signal discontinuous system model of BQZSDC gets converted into an SM continuous system and is given as follows:

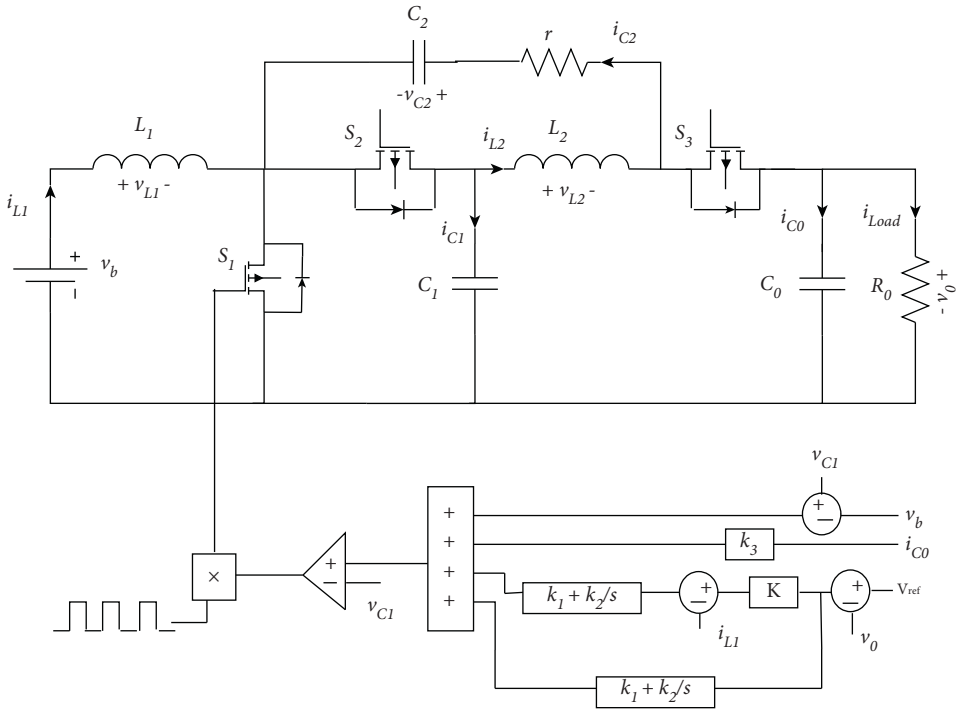

Figure 5: BQZSDC with the FF-DISM controller.

$$\frac{d}{dt}\begin{bmatrix} \hat{i}_{L1} \\ \hat{i}_{L2} \\ \hat{v}_{C1} \\ \hat{v}_{C2} \\ \hat{v}_0 \end{bmatrix} = \begin{bmatrix} \dfrac{(v_b - v_{C1})}{L_1} \\ \dfrac{(v_{C1} - v_0)}{L_2} \\ \dfrac{(i_{L1} - i_{L2})}{C_1} + \dfrac{(v_0 - v_{C1} - v_{C2})}{C_1 r} \\ \dfrac{(v_0 - v_{C1} - v_{C2})}{C_2 r} \\ \dfrac{-v_0}{C_0 R_L} + \dfrac{i_{L2}}{C_0} - \dfrac{(v_0 - v_{C1} - v_{C2})}{C_0 r} \end{bmatrix} + \begin{bmatrix} \dfrac{v_{C1}}{L_1} \\ \dfrac{(v_0 - v_{C2} - i_{L2} r)}{L_2} \\ \dfrac{-i_{L1}}{C_1} - \dfrac{(v_0 - v_{C1} - v_{C2})}{C_1 r} \\ \dfrac{i_{L2}}{C_2} - \dfrac{(v_0 - v_{C1} - v_{C_2})}{C_2 r} \\ \dfrac{-i_{L2}}{C_0} + \dfrac{(v_0 - v_{C1} - v_{C_2})}{C_0 r} \end{bmatrix} u_{eq}. \tag{33}$$

Then, substituting the equivalent control signal (23) in (33) gives the following:

$$\begin{bmatrix} \frac{\mathrm{d}\hat{i}_{L1}}{\mathrm{d}t} \\ \frac{\mathrm{d}\hat{i}_{L2}}{\mathrm{d}t} \\ \frac{\mathrm{d}\hat{v}_{C1}}{\mathrm{d}t} \\ \frac{\mathrm{d}\hat{v}_{C2}}{\mathrm{d}t} \\ \frac{\mathrm{d}\hat{v}_{0}}{\mathrm{d}t} \end{bmatrix} = \begin{bmatrix} \frac{(v_b - v_{C1})}{L_1} + \frac{1}{L_1}\left(-i_{C_0}k_3 - v_b + v_{C1} + k_1(x_1 + x_2) + k_2\int(x_1 + x_2)\mathrm{d}t\right) \\ \frac{(v_{C1} - v_0)}{L_2} + \frac{(v_0 - v_{C2} - i_{L2}r)}{L_2}\left(\frac{\left(-i_{C_0}k_3 - v_b + v_{C1} + k_1(x_1 + x_2) + k_2\int(x_1 + x_2)\mathrm{d}t\right)}{v_{C1}}\right) \\ \frac{i_{L1} - i_{L2}}{C_1} + \frac{(v_0 - v_{C1} - v_{C2})}{C_1 r} + \left(\frac{-i_{L1}}{C_1} - \frac{(v_0 - v_{C1} - v_{C2})}{C_1 r}\right)\left(\frac{\left(-i_{C_0}k_3 - v_b + v_{C1} + k_1(x_1 + x_2) + k_2\int(x_1 + x_2)\mathrm{d}t\right)}{v_{C1}}\right) \\ \frac{(v_0 - v_{C1} - v_{C2})}{C_2 r} + \left(\frac{i_{l_2}}{C_2} - \frac{(v_0 - v_{C1} - v_{C2})}{C_2 r}\right)\left(\frac{\left(-i_{C_0}k_3 - v_b + v_{C1} + k_1(x_1 + x_2) + k_2\int(x_1 + x_2)\mathrm{d}t\right)}{v_{C1}}\right) \\ \frac{-v_0}{C_o R_0} + \frac{i_{L2}}{C_0} - \frac{(v_0 - v_{C1} - v_{C2})}{C_0 r} + \left(\frac{-i_{L2}}{C_o} + \frac{(v_0 - v_{C1} - v_{C2})}{C_0 r}\right)\left(\frac{\left(-i_{C_0}k_3 - v_b + v_{C1} + k_1(x_1 + x_2) + k_2\int(x_1 + x_2)\mathrm{d}t\right)}{v_{C1}}\right) \end{bmatrix}. \tag{34}$$

3.5.2. Equilibrium-Point Analysis. Consider that the ideal sliding dynamics finally settle at a stable equilibrium point on the sliding surface. If there is no input or loading disturbance, the system's dynamics will remain unchanged at this equilibrium point (steady state); i.e., the steady-state values at that operating point are given as follows:

$$\begin{cases} I_{L1} = \dfrac{V_0^2}{V_b R_L}, \\ I_{L2} = \dfrac{V_0}{R_L}, \\ V_{C1} = \dfrac{V_0 + V_b}{2}, \\ V_{C2} = \dfrac{V_0 - V_b}{2}, \\ V_0 = V_{\text{ref}}. \end{cases} \tag{35}$$

3.5.3. Linearization of Ideal Sliding Dynamic. The ideal SM continuous BQZSDC system's small-signal state model was developed at stable equilibrium operating point (35).

$$\frac{\mathrm{d}(I_{L1} + \bar{i}_{L1})}{\mathrm{d}t} = \frac{(V_b - V_{C1} - \bar{v}_{C1})}{L_1} + \frac{1}{L_1}\left(-C_0 k_3 \frac{\mathrm{d}(V_0 + \bar{v}_0)}{\mathrm{d}t} - V_b + V_{C1} + \bar{v}_{C1} - k_1 K \bar{v}_0 - k_1 \bar{i}_{L1} - k_2 K \int \bar{v}_0 \mathrm{d}t - k_2 \int \bar{i}_{L1} \mathrm{d}t\right),$$

$$\frac{\mathrm{d}(I_{L2} + \bar{i}_{L2})}{\mathrm{d}t} = \frac{V_{C1} + \bar{v}_{C1}}{L_2} - \frac{V_0 + \bar{v}_0}{L_2} + \frac{(V_0 + \bar{v}_0 - V_{C2} - \bar{v}_{C2} - I_{L2} r - \bar{i}_{L2} r)}{L_2} \times \left(\frac{-C_0 k_3 (\mathrm{d}(V_0 + \bar{v}_0)/\mathrm{d}t) - V_b + V_{C1} + \bar{v}_{C1} - k_1 K \bar{v}_0 - k_1 \bar{i}_{L1} - k_2 K \int \bar{v}_0 \mathrm{d}t - k_2 \int \bar{i}_{L1} \mathrm{d}t}{V_{c_1}}\right),$$

$$\frac{\mathrm{d}(V_{C1} + \bar{v}_{C1})}{\mathrm{d}t} = \frac{I_{L1} + \bar{i}_{L1} - I_{L2} - \bar{i}_{L2}}{C_1} + \frac{(V_0 + \bar{v}_0 - V_{C1} - \bar{v}_{C1} - V_{C2} - \bar{v}_{C2})}{C_1 r} + \left(\frac{-I_{L1} - \bar{i}_{L1}}{C_1} - \frac{(V_0 - \bar{v}_0 - V_{C1} - \bar{v}_{C1} - V_{C2} - \bar{v}_{C2})}{C_1 r}\right) \times \left(\frac{-C_0 k_3 (\mathrm{d}(V_0 + \bar{v}_0)/\mathrm{d}t) - V_b + V_{C1} + \bar{v}_{C1} - k_1 K \bar{v}_0 - k_1 \bar{i}_{L1} - k_2 K \int \bar{v}_0 \mathrm{d}t - k_2 \int \bar{i}_{L1} \mathrm{d}t}{V_{C1}}\right),$$

$$\frac{\mathrm{d}(V_{C2} + \bar{v}_{C2})}{\mathrm{d}t} = \frac{(V_0 - \bar{v}_0 - V_{C1} - \bar{v}_{C1} - V_{C2} - \bar{v}_{C2})}{C_2 r} + \left(\frac{I_{L2} + \bar{i}_{l_2}}{C_2} - \frac{(V_0 + \bar{v}_0 - V_{C1} - \bar{v}_{C1} - V_{C2} - \bar{v}_{C2})}{C_2 r}\right) \times \left(\frac{-C_0 k_3 (\mathrm{d}(V_0 + \bar{v}_0)/\mathrm{d}t) - V_b + V_{C1} + \bar{v}_{C1} - k_1 K \bar{v}_0 - k_1 \bar{i}_{L1} - k_2 K \int \bar{v}_0 \mathrm{d}t - k_2 \int \bar{i}_{L1} \mathrm{d}t}{V_{C1}}\right),$$

$$\frac{\mathrm{d}(V_0 + \bar{v}_0)}{\mathrm{d}t} = \frac{-V_0 - \bar{v}_0}{C_o R_0} + \frac{I_{L2} + \bar{i}_{L2}}{C_0} - \frac{(V_0 + \bar{v}_0 - V_{C1} - \bar{v}_{C1} - V_{C2} - \bar{v}_{C2})}{C_0 r} + \left(\frac{-I_{L2} - i_{L2}}{C_o} + \frac{(V_0 + \bar{v}_0 - V_{C1} - \bar{v}_{C1} - V_{C2} - \bar{v}_{C2})}{C_0 r}\right) \times \left(\frac{-C_0 k_3 (\mathrm{d}(V_0 + \bar{v}_0)/\mathrm{d}t) - V_b + V_{C1} + \bar{v}_{C1} - k_1 K \bar{v}_0 - k_1 \bar{i}_{L1} - k_2 K \int \bar{v}_0 \mathrm{d}t - k_2 \int \bar{i}_{L1} \mathrm{d}t}{V_{C1}}\right). \tag{36}$$

The above equations are derived by assuming the validity of the following conditions: $v_b = V_b$, $V\text{ref} - V_0 = 0$, $I_{\text{ref}} = I_{L1} = K(v_{\text{ref}} - V_0)$ and $I_{L1} \gg \bar{i}_{L1}$, $I_{L2} \gg \bar{i}_{L2}$, $V_{C1} \gg \bar{v}_{C1}$, $V_{C2} \gg \bar{v}_{C2}$, $V_0 \gg \bar{v}_0$, by considering only AC terms. The linearized dynamic model at equilibrium point (35) is given by the following:

$$
\begin{aligned}
\frac{\mathrm{d}\bar{i}_{L1}}{\mathrm{d}t} &= \frac{-\bar{v}_{C1}}{L_1} + \frac{1}{L_1}\left(-k_3\left(\frac{-\bar{v}_0}{R_0} + \bar{i}_{L2}\right) + \bar{v}_{C1} - k_1 K\bar{v}_0 - k_1\bar{i}_{L1} - k_2 K\int \bar{v}_0\mathrm{d}t - k_2\int \bar{i}_{L1}\mathrm{d}t\right),\\
\frac{\mathrm{d}\bar{i}_{L2}}{\mathrm{d}t} &= \frac{\bar{v}_{C1}}{L_2} - \frac{\bar{v}_0}{L_2} + \frac{(V_0 + \bar{v}_0 - V_{C2} - \bar{v}_{C2} - I_{L2}r - \bar{i}_{L2}r)}{L_2}\\
&\quad\times\left(\frac{k_3(\bar{v}_0/R_0) - k_3\bar{i}_{L2} - V_b + V_{C1} + \bar{v}_{C1} - k_1 K\bar{v}_0 - k_1\bar{i}_{L1} - k_2 K\int \bar{v}_0\mathrm{d}t - k_2\int \bar{i}_{L1}\mathrm{d}t}{V_{c_1}}\right),\\
\frac{\mathrm{d}(V_{C1} + \bar{v}_{C1})}{\mathrm{d}t} &= \frac{\bar{i}_{L1} - \bar{i}_{L2}}{C_1} + \frac{(\bar{v}_0 - \bar{v}_{C1} - \bar{v}_{C2})}{C_1 r} + \left(\frac{-I_{L1} - \bar{i}_{L1}}{C_1} - \frac{(V_0 - \bar{v}_0 - V_{C1} - \bar{v}_{C1} - V_{C2} - \bar{v}_{C2})}{C_1 r}\right)\\
&\quad\times\left(\frac{k_3(\bar{v}_0/R_0) - k_3\bar{i}_{L2} - V_b + V_{C1} + \bar{v}_{C1} - k_1 K\bar{v}_0 - k_1\bar{i}_{L1} - k_2 K\int \bar{v}_0\mathrm{d}t - k_2\int \bar{i}_{L1}\mathrm{d}t}{V_{C1}}\right),\\
\frac{\mathrm{d}\bar{v}_{C2}}{\mathrm{d}t} &= \frac{(\bar{v}_0 - \bar{v}_{C1} - \bar{v}_{C2})}{C_2 r} + \left(\frac{I_{L2} + \bar{i}_{l_2}}{C_2} - \frac{(V_0 + \bar{v}_0 - V_{C1} - \bar{v}_{C1} - V_{C2} - \bar{v}_{C2})}{C_2 r}\right)\\
&\quad\times\left(\frac{k_3(\bar{v}_0/R_0) - k_3\bar{i}_{L2} - V_b + V_{C1} + \bar{v}_{C1} - k_1 K\bar{v}_0 - k_1\bar{i}_{L1} - k_2 K\int \bar{v}_0\mathrm{d}t - k_2\int \bar{i}_{L1}\mathrm{d}t}{V_{C1}}\right),\\
\frac{\mathrm{d}(\bar{v}_0)}{\mathrm{d}t} &= \frac{-\bar{v}_0}{C_o R_0} + \frac{\bar{i}_{L2}}{C_0} - \frac{(\bar{v}_0 - \bar{v}_{C1} - \bar{v}_{C2})}{C_0 r} + \left(\frac{-I_{L2} - i_{L2}}{C_o} + \frac{(V_0 + \bar{v}_0 - V_{C1} - \bar{v}_{C1} - V_{C2} - \bar{v}_{C2})}{C_0 r}\right)\\
&\quad\times\left(\frac{k_3(\bar{v}_0/R_0) - k_3\bar{i}_{L2} - V_b + V_{C1} + \bar{v}_{C1} - k_1 K\bar{v}_0 - k_1\bar{i}_{L1} - k_2 K\int \bar{v}_0\mathrm{d}t - k_2\int \bar{i}_{L1}\mathrm{d}t}{V_{C1}}\right).
\end{aligned}
\tag{37}
$$

By rearranging the above equations in standard form, we get the following:

$$\begin{cases} \dfrac{\mathrm{d}\widetilde{i}_{L1}}{\mathrm{d}t} = \alpha_{11}\widetilde{i}_{L1} + \alpha_{12}\widetilde{i}_{L2} + \alpha_{13}\widetilde{v}_{C1} + \alpha_{14}\widetilde{v}_{C2} + \alpha_{15}\widetilde{v}_0 + \alpha_{16}\int \widetilde{i}_{L1}\mathrm{d}t + \alpha_{17}\int \widetilde{v}_0\mathrm{d}t, \\ \dfrac{\mathrm{d}\widetilde{i}_{L2}}{\mathrm{d}t} = \alpha_{21}\widetilde{i}_{L1} + \alpha_{22}\widetilde{i}_{L2} + \alpha_{23}\widetilde{v}_{C1} + \alpha_{24}\widetilde{v}_{C2} + \alpha_{25}\widetilde{v}_0 + \alpha_{26}\int \widetilde{i}_{L1}\mathrm{d}t + \alpha_{27}\int \widetilde{v}_0\mathrm{d}t, \\ \dfrac{\mathrm{d}\widetilde{v}_{C1}}{\mathrm{d}t} = \alpha_{31}\widetilde{i}_{L1} + \alpha_{32}\widetilde{i}_{L2} + \alpha_{33}\widetilde{v}_{C1} + \alpha_{34}\widetilde{v}_{C2} + \alpha_{35}\widetilde{v}_0 + \alpha_{36}\int \widetilde{i}_{L1}\mathrm{d}t + \alpha_{37}\int \widetilde{v}_0\mathrm{d}t, \\ \dfrac{\mathrm{d}\widetilde{v}_{C2}}{\mathrm{d}t} = \alpha_{41}\widetilde{i}_{L1} + \alpha_{42}\widetilde{i}_{L2} + \alpha_{43}\widetilde{v}_{C1} + \alpha_{44}\widetilde{v}_{C2} + \alpha_{45}\widetilde{v}_0 + \alpha_{46}\int \widetilde{i}_{L1}\mathrm{d}t + \alpha_{47}\int \widetilde{v}_0\mathrm{d}t, \\ \dfrac{\mathrm{d}\widetilde{v}_0}{\mathrm{d}t} = \alpha_{51}\widetilde{i}_{L1} + \alpha_{52}\widetilde{i}_{L2} + \alpha_{53}\widetilde{v}_{C1} + \alpha_{54}\widetilde{v}_{C2} + \alpha_{55}\widetilde{v}_0 + \alpha_{56}\int \widetilde{i}_{L1}\mathrm{d}t + \alpha_{57}\int \widetilde{v}_0\mathrm{d}t, \\ \dfrac{\mathrm{d}\left[\int \widetilde{i}_{L1}\mathrm{d}t\right]}{\mathrm{d}t} = \alpha_{61}\widetilde{i}_{L1} + \alpha_{62}\widetilde{i}_{L2} + \alpha_{63}\widetilde{v}_{C1} + \alpha_{64}\widetilde{v}_{C2} + \alpha_{65}\widetilde{v}_0 + \alpha_{66}\int \widetilde{i}_{L1}\mathrm{d}t + \alpha_{67}\int \widetilde{v}_0\mathrm{d}t, \\ \dfrac{\mathrm{d}\left[\int \widetilde{v}_0\mathrm{d}t\right]}{\mathrm{d}t} = \alpha_{71}\widetilde{i}_{L1} + \alpha_{72}\widetilde{i}_{L2} + \alpha_{73}\widetilde{v}_{C1} + \alpha_{74}\widetilde{v}_{C2} + \alpha_{75}\widetilde{v}_0 + \alpha_{76}\int \widetilde{i}_{L1}\mathrm{d}t + \alpha_{17}\int \widetilde{v}_0\mathrm{d}t. \end{cases} \tag{38}$$

The characteristic equation of the linearized system is given by the following:

$$\begin{vmatrix} s-\alpha_{11} & -\alpha_{12} & 0 & 0 & -\alpha_{15} & -\alpha_{16} & -\alpha_{17} \\ -\alpha_{21} & s-\alpha_{22} & -\alpha_{23} & -\alpha_{24} & -\alpha_{25} & -\alpha_{26} & -\alpha_{27} \\ -\alpha_{31} & -\alpha_{32} & s-\alpha_{33} & -\alpha_{34} & -\alpha_{35} & -\alpha_{36} & -\alpha_{37} \\ -\alpha_{41} & -\alpha_{42} & -\alpha_{43} & s-\alpha_{44} & -\alpha_{45} & -\alpha_{46} & -\alpha_{47} \\ -\alpha_{51} & -\alpha_{52} & -\alpha_{53} & -\alpha_{54} & s-\alpha_{55} & -\alpha_{56} & -\alpha_{57} \\ -1 & 0 & 0 & 0 & 0 & s & 0 \\ 0 & 0 & 0 & 0 & -1 & 0 & s \end{vmatrix} = s^7 + p_1 s^6 + p_2 s^5 + p_3 s^4 + p_4 s^3 + p_5 s^2 + p_6 s + p_7 = 0, \tag{39}$$

where

$$
\begin{cases}
\alpha_{11} = \dfrac{-k_1}{L_1}, \\
\alpha_{12} = \dfrac{-k_1}{L_1}, \\
\alpha_{13} = 0, \\
\alpha_{14} = 0, \\
\alpha_{15} = \dfrac{-k_1 - k_1 K R_0}{L_1 R_0}, \\
\alpha_{16} = \dfrac{-k_1}{L_1}, \\
\alpha_{17} = \dfrac{-k_1 K}{L_1}, \\
\alpha_{21} = \dfrac{-K(V_0 - V_{C1} - I_{L2}r)}{L_2 V_{C1}}, \\
\alpha_{22} = \dfrac{-r(V_{C1} - V_b) - k_2(V_0 - V_{C1} - I_{L2}r)}{L_2 V_{C1}}, \\
\alpha_{23} = \dfrac{(V_0 - V_{C1} - I_{L2}r)}{L_2 V_{C1}}, \\
\alpha_{24} = \dfrac{(V_0 - V_{C1} - I_{L2}r)}{L_2 V_{C1}} + \dfrac{V_b - V_{C1}}{L_2 V_{C1}}, \\
\alpha_{25} = \dfrac{-1}{L_2} + \left[\dfrac{k_2 - k_1 K}{R_0}\right]\left[\dfrac{(V_0 - V_{C1} - I_{L2}r)}{L_2 V_{C1}}\right] + \dfrac{(V_{C1} - V_b)}{L_2 V_{C1}}, \\
\alpha_{26} = \dfrac{-k_2(V_0 - V_{C1} - I_{L2}r)}{L_2 V_{C1}}, \\
\alpha_{27} = \dfrac{-k_2 K(V_0 - V_{C1} - I_{L2}r)}{L_2 V_{C1}}, \\
\alpha_{31} = \dfrac{-k_2 I_{L1} r - V_b}{V_{C1} r C_1}, \\
\alpha_{32} = \dfrac{k_2 I_{L1} r - V_b}{C_1 V_{C1} r}, \\
\alpha_{33} = \dfrac{-V_b - I_{L1} r}{C_1 V_{C1} r}, \\
\alpha_{34} = \dfrac{-V_b}{C_1 V_{C1} r}, \\
\alpha_{35} = \left[\dfrac{k_2 - k_1 K R_0}{R_0}\right]\left[\dfrac{(V_0 - V_{C1} - I_{L1}r) + V_b}{L_2 V_{C1}}\right], \\
\alpha_{36} = \dfrac{k_2 I_{L1}}{C_1 V_{C1}}, \\
\alpha_{37} = \dfrac{k_2 K I_{L1}}{C_1 V_{C1}},
\end{cases}
$$

$$
\begin{cases}
\alpha_{41} = \dfrac{-k_2 r I_{L2}}{C_2 V_{C1}}, \\
\alpha_{42} = \dfrac{-k_2 I_{L2} r + V_{C1} - V_b}{C_2 V_{C1} r}, \\
\alpha_{43} = \dfrac{I_{L2} r - V_b}{C_2 V_{C1} r}, \\
\alpha_{44} = \dfrac{-V_b}{C_2 V_{C1} r}, \\
\alpha_{45} = \dfrac{-1}{C_2} + \left[\dfrac{k_2 - k_1 K}{R_0}\right]\left[\dfrac{(V_0 - V_{C1} - I_{L2}r)}{C_2 V_{C1}}\right], \\
\alpha_{46} = \dfrac{K_2 I_{L2}}{C_2 V_{C1}}, \\
\alpha_{47} = \dfrac{K K_2 I_{L2}}{C_2 V_{C1}}, \\
\alpha_{51} = \dfrac{k_1 I_{L2} r}{C_0 V_{C1}}, \\
\alpha_{52} = \dfrac{k_2 I_{L2} r + V_b}{C_0 V_{C1} r}, \\
\alpha_{53} = \dfrac{I_{L2} r + V_b}{C_0 V_{C1} r}, \\
\alpha_{54} = \dfrac{V_b}{C_0 V_{C1} r}, \\
\alpha_{55} = \dfrac{-1}{C_0} + \left[\dfrac{k_2 - k_1 K}{R_0}\right]\left[\dfrac{(V_0 - V_{C1} - I_{L2}r)}{C_2 V_{C1}}\right], \\
\alpha_{56} = \dfrac{K_2 I_{L2}}{C_0 V_{C1}}, \\
\alpha_{57} = \dfrac{K_2 K I_{L2}}{C_0 V_{C1}}, \\
\alpha_{61} = 1, \\
\alpha_{62} = 0, \\
\alpha_{63} = 0, \\
\alpha_{64} = 0, \\
\alpha_{65} = 0, \\
\alpha_{66} = 0, \\
\alpha_{67} = 0, \\
\alpha_{71} = 0, \\
\alpha_{72} = 0, \\
\alpha_{73} = 0, \\
\alpha_{74} = 0, \\
\alpha_{75} = 1, \\
\alpha_{76} = 0, \\
\alpha_{77} = 0.
\end{cases}
\tag{40}
$$

The range of control gains obtained by applying the Routh–Hurwitz criterion to characteristic equation (39) is as follows:

$$\begin{cases} p_1 > 0, \\ p_2 > \dfrac{p_3}{p_1}, \\ p_3 > p_1 p_4 - p_5, \\ p_4 > \dfrac{(p_1 p_2 - p_3) p_5 - (p_1 p_2 - p_7) + p_5 p_1}{p_1}, \\ p_5 > \dfrac{(p_1 p_2 - p_3) p_3 - p_1^2 p_6 - p_1 p_7}{p_1 p_2 - p_3 + p_1}, \\ p_6 > \dfrac{(p_1 p_2 - p_3) p_3 - p_1^2 p_4 - p_1 p_7 - (p_1 p_2 - p_3 + p_1) p_5}{p_1^2}, \\ P_7 > 0. \end{cases} \tag{41}$$

The stability of the system is found by substituting (40) in (41). This, coupled with the existing condition (31) and (32), constitutes the foundation for selecting and designing the controller's control gains in conjunction with the converter's specified requirements.

3.6. Selection of Control Gains. The sliding coefficients were chosen after analyzing the effect of changing the control gains on the output voltage.

The subsequent conclusions were attained:

(1) The increase in K minimizes the steady-state error but increases the settling time by making the transient response more oscillatory

(2) The slope of voltage responses can be increased or decreased by changing k_1

(3) The increment in k_2 reduces the settling time but raises the steady-state error

(4) The increment in k_3 reduces transient response overshoot while slightly increasing settling time

The values of k_1, k_2, and k_3 are selected based on the above observations until the controller provides the required performance.

4. Results and Discussion

The proposed control technique was developed in MATLAB/Simulink and tested on a prototype. These details are addressed in the subsections that follow.

4.1. Simulation Results. The efficiency and performance of the proposed controller for the converter are examined based on a set of simulations. Even though the controller was developed using the boost mode approach, it can also be used in buck mode. This section analyzes the converter's responses for reference and load changes in both buck and boost modes.

4.1.1. Reference Change. The effect of changing the reference voltage on the controller and its tracking ability is analyzed. The reference voltage was varied from 48 V to 36 V at 0.2 sec, and it is observed that the $v_0$is tracking the new reference of 36 V, as shown in Figure 6. Furthermore, it can be seen that at 0.4 sec, the voltage is restored to 48 V, and the controller tracks the output voltage in line with the reference voltage of 48 V.

The parameters of the converter are mentioned in Table 1.

The converter can operate in step-up and step-down modes, thereby enabling the battery to charge or discharge depending on the power flow. The system was connected to a PV source interface with a load attached to the common bus. The load is desired to be catered for at a constant voltage of 48 V. If the PV power is more than the load power, the BQZSDC is switched to buck mode, and the excess energy is used to charge the battery. If the PV power is less than the load power required, the BQZSDC goes into boost mode, and the battery is discharged to make up the difference.

As a part of this work, a 12 V battery is considered, and the output reference voltage is taken as 48 V. The PV system acts as a constant source (operating at constant irradiation) current of 4.17 A supplying 200 W, connected at the load side of the BQZDC. The converter performance was observed under load variations.

4.1.2. Boost Mode (Discharging Mode). In this mode, the battery starts discharging through the converter supplying the deficit power to maintain the power balance and a stable output voltage. As shown in Figure 7, the initial load demand is 5.2 A, out of which the PV source is supplying 4.17 A. The converter provides the remaining current of 1.03 A (stepping down the battery current from 4.16 A) and maintains the load voltage at 48 V. The load current was observed to be enhanced to 6.25 A at time $t = 0.2$ sec. The results show that the excess current of 2.08 A was supplied by the converter (stepping down the battery current from 8.33 A). Moreover, at $t = 0.4$ sec, the load current returns to 5.2 A, and the converter supplies excess current even under this condition. Figure 8 shows the variation of SOC of battery and load voltage.

4.1.3. Buck Mode (Charging Mode). In this mode, the battery starts charging through the converter absorbing the excess power to maintain the power balance and a stable output voltage. Initially, the load current was 4.17 A which was exactly catered for by the PV. Thus, the battery remains idle with no current being supplied or absorbed. The load demand decreased to 2.08 A at $t = 0.2$ sec, and as shown in Figure 9, the surplus current absorbed by the battery to

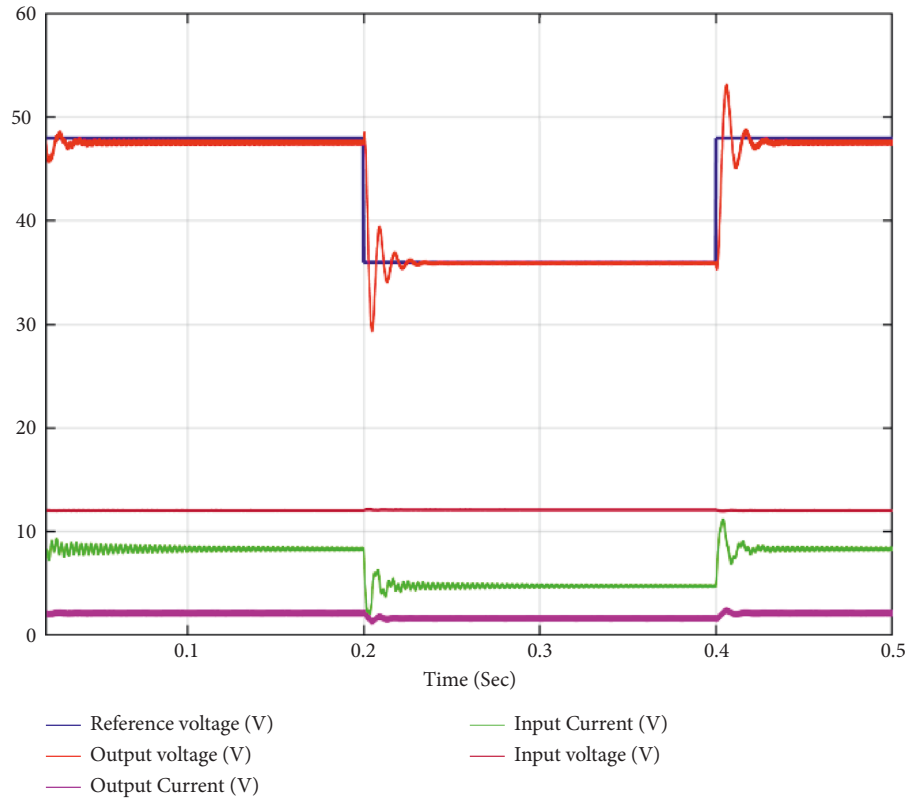

Figure 6: Waveforms of BQZSD under reference output voltage variation with double-integral sliding mode controller.

Table 1: Parameters of the converter.

Parameter	Value
Power	100 W
Output voltage V_0	48 V
Battery voltage V_b	12 V
Inductors L_1 and L_2	1 mH, 3.3 mH
Capacitors C_1 and C_2	100 μF
Resistor r	0.216 Ω
Capacitor C_0	470 μF

charge itself and the battery current is negative. Consequently, at $t = 0.4$ sec, the load current is increased again to 4.17 A, and at this point, the battery and the converter remain idle without any current. The load voltage is sustained at 48 V throughout, and Figure 10 shows the variation of SOC of battery and load voltage profile.

4.2. Hardware Implementation and Results. The laboratory setup for the hardware implementation of the proposed work is shown in Figure 11.

A programmable DC power supply (Chroma-62020H-150S) from Chroma was employed as a PV source. Three LEM voltage sensors (LV25-P/SP213205) and two current sensors (LA55-P14316) were used to sense different voltages and currents. Outputs of sensors were given to dSPACE-1104 ADC channels with appropriate gain. This was used to implement the proposed control algorithm.

To capture the experimental results, RIGOL-DS1054 was used. The presented control algorithm was implemented by generating three gate pulses with an adjustable duty cycle using dSPACE-1104. A distinct gate pulse was given to switch the parallel-connected load to change the load.

The experimental tests were carried out in fewer than two conditions: (i) change in the reference voltage and (ii) change in the load (boost and buck mode).

4.2.1. Reference Change. The reference voltage is varied from 48 V to 36 V at a particular time, and it is shown that the output voltage v_0 is tracking the new reference of 36 V, as shown in Figure 12. Furthermore, it can be seen that the reference voltage has been restored to 48 V, and the controller tracks the output voltage in line with the reference voltage of 48 V.

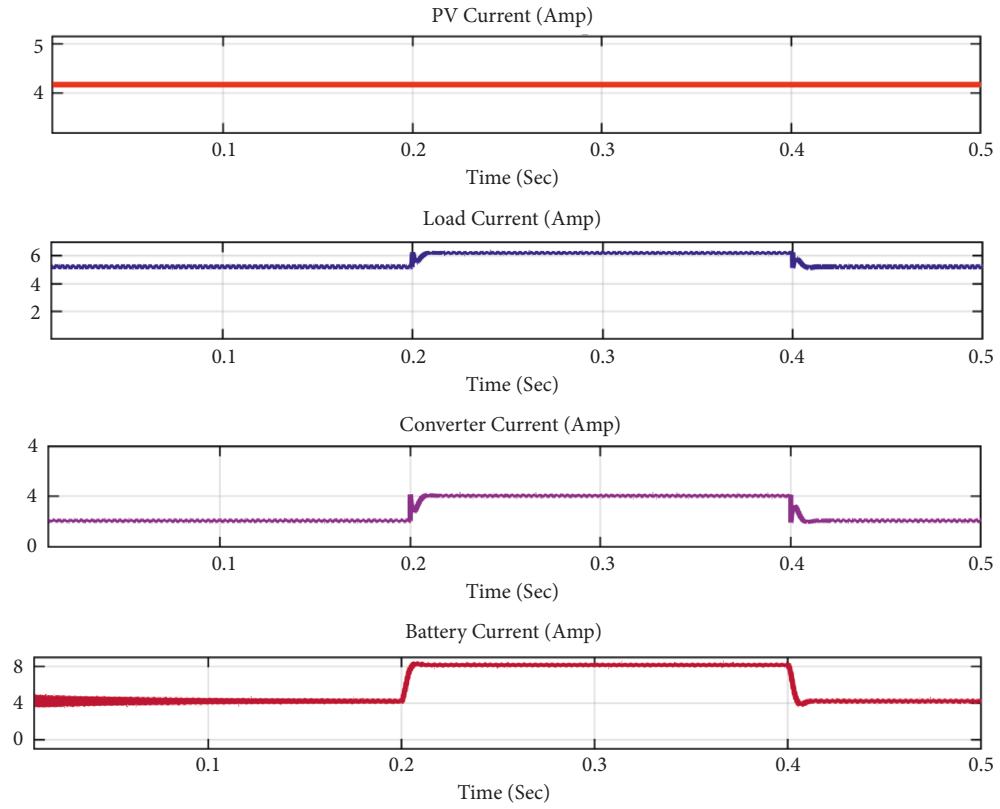

Figure 7: Different currents waveforms of BQZSDC when the load varied from 5.208 A to 6.25 A and vice versa in boost mode.

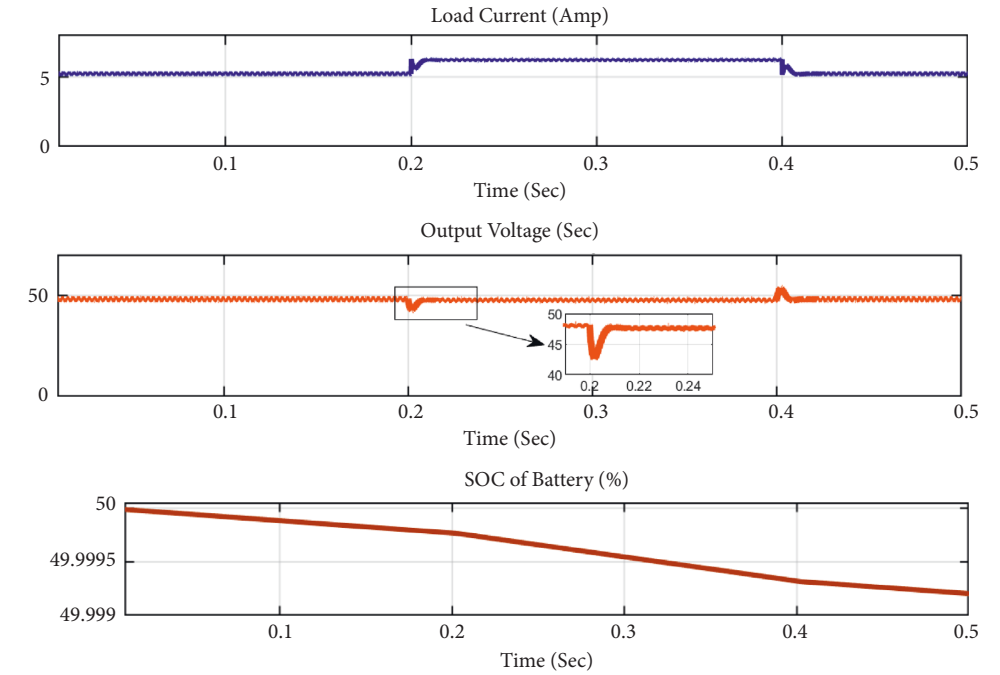

Figure 8: Output voltage and SOC of the battery when the load varied from 5.208 A to 6.25 A and vice versa in boost mode.

The converter can work in both modes, making it easier to charge or discharge the battery depending on the power flow.

4.2.2. Boost Mode (Discharging Mode). The battery begins discharging through the converter in boost mode, which supplies the deficit power to keep the power balance and

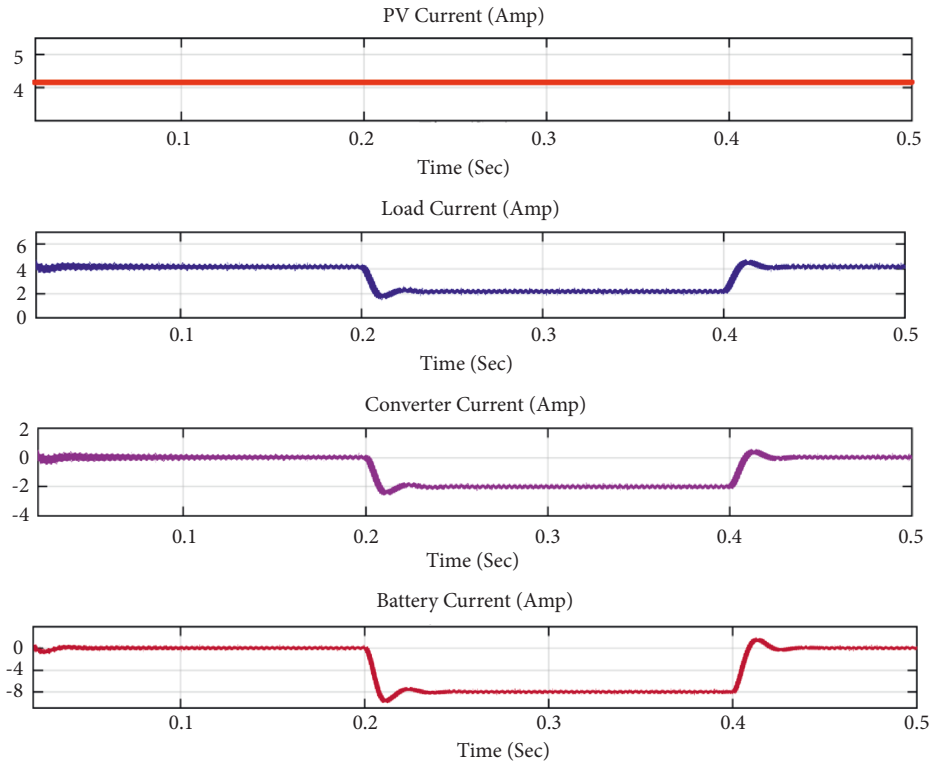

Figure 9: Different current waveforms when the load varied from 4.17 A to 2.08 A and vice versa in buck mode.

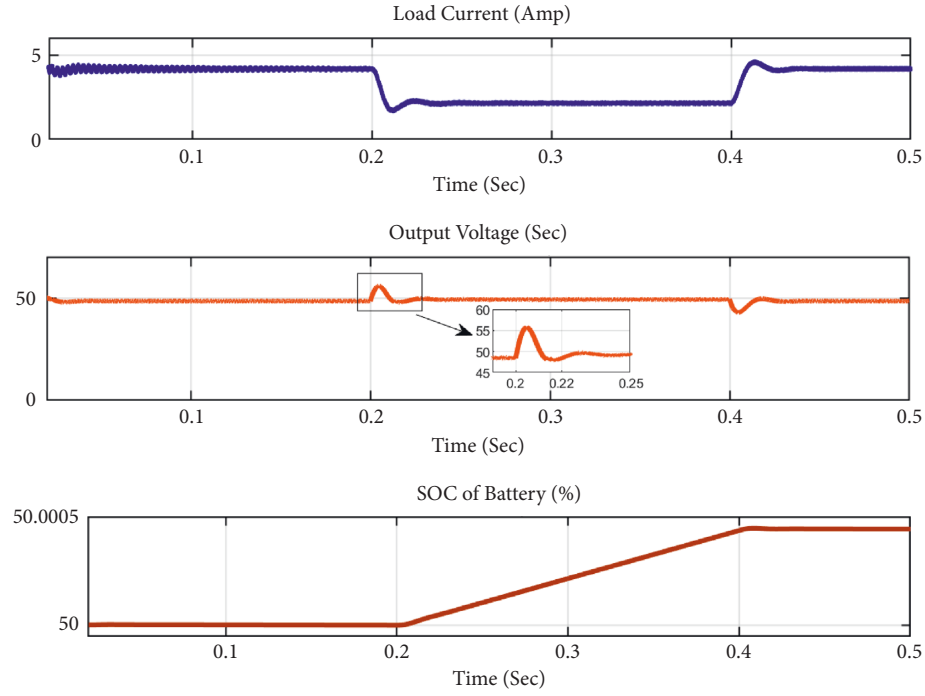

Figure 10: Output voltage and SOC of the battery when load varied from 4.17 A to 2.08 A and vice versa in buck mode.

output voltage stable. The initial load requirement is 5.2 A, as illustrated in Figure 13, with the PV source contributing 4.17 A. The converter supplies 1.03 A of the remaining current (stepping down the battery current from 4.16 A). As load demand increases, the battery supplies even more current while keeping the load voltage at 48 V.

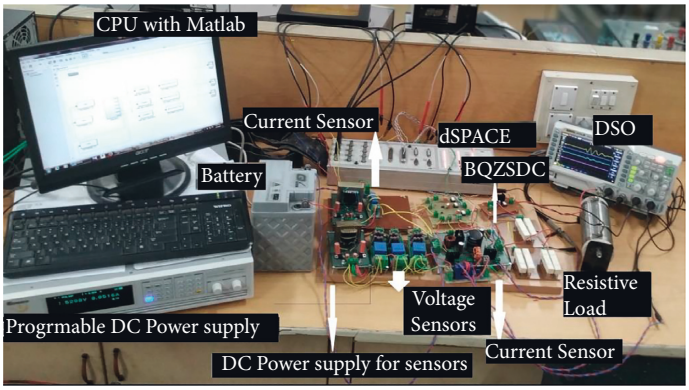

Figure 11: Experimental setup for hardware implementation.

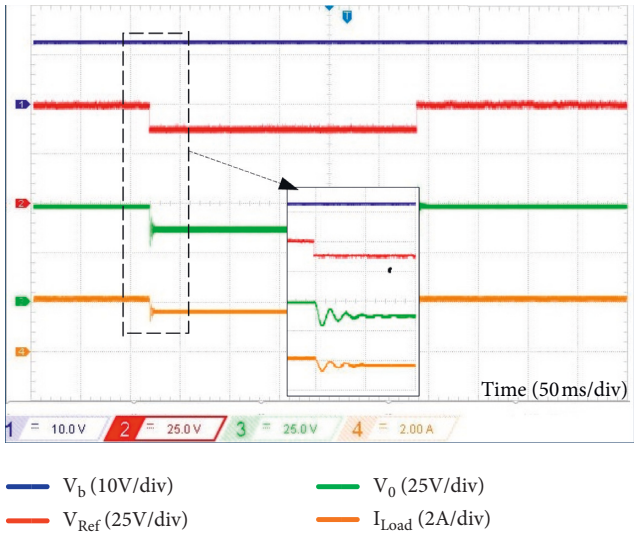

Figure 12: Hardware results when the reference voltage is varied from 48 V to 36 V and vice versa.

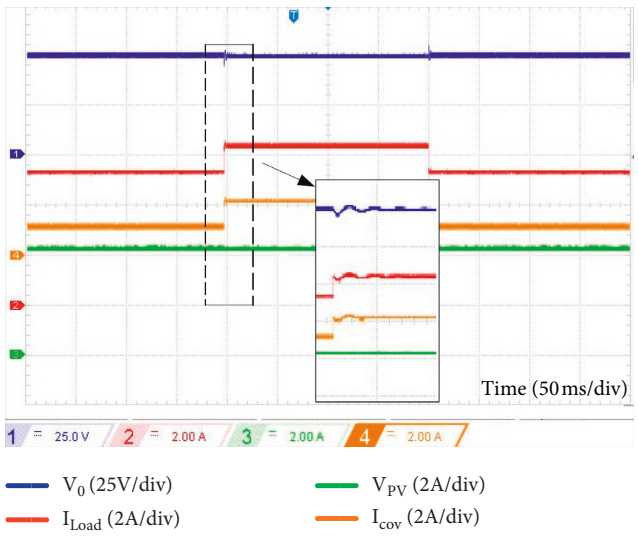

Figure 13: Hardware results when the load current was varied from 5.208 to 6.25 V and vice versa (boost mode).

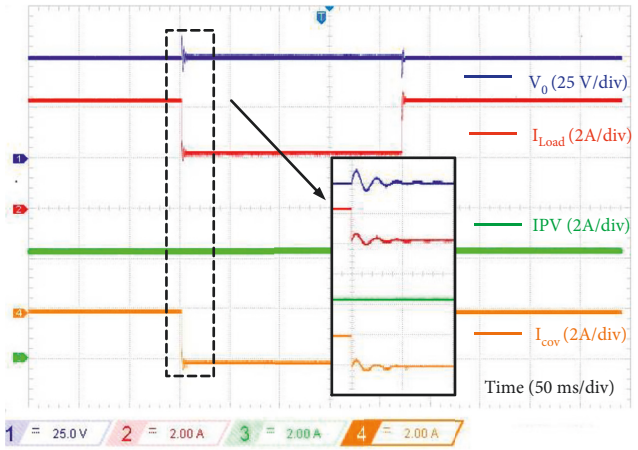

Figure 14: Hardware results when the load current is varied from 4.17 A to 2.08 A and vice versa (buck mode).

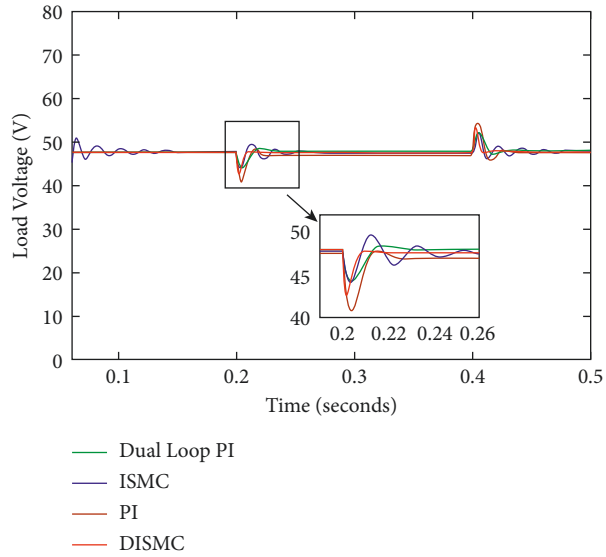

Figure 15: Waveforms of the load voltage of BQZSDC with different control techniques in boost mode for load change.

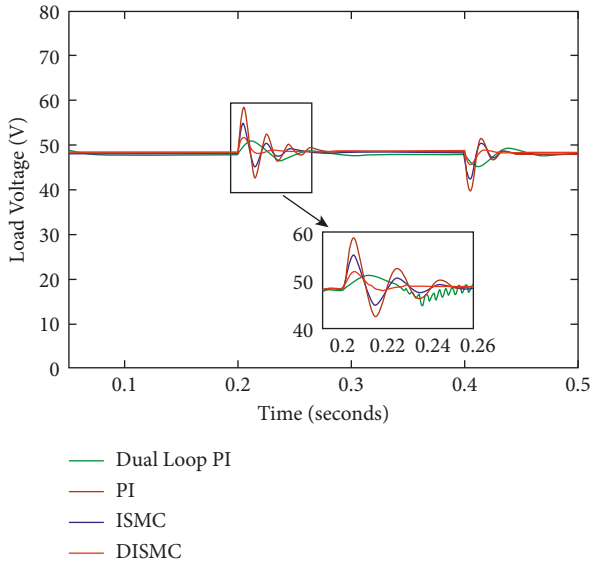

Figure 16: Waveforms of the load voltage of BQZSDC with different control techniques in buck mode for load change.

Table 2: Time-domain specifications in boost mode.

Controller	Rise time (ms)	% peak undershoot (%)	Settling time (ms)
PI controller	9.7	14.5	23
Dual-loop PI controller	8	6.1	20
Integral SMC	1.2	6	25
Double-integral SMC	0.8	7.1	7

Table 3: Time-domain specifications in buck mode.

Controller	Rise time (ms)	% peak overshoot (%)	Settling time (ms)
PI controller	9.7	20.8	45
Dual-loop PI controller	8	6.1	35
Integral SMC	1.2	14.5	29
Double-integral SMC	0.8	8.3	15

4.2.3. Buck Mode (Charging Mode). The battery begins charging through the converter in buck mode, absorbing excess power to keep the power balance and output voltage stable. Initially, the load current is 4.17 A, which the PV can handle perfectly. As a result, the battery stays uncharged, and no current is delivered or absorbed. As the load demand decreases, the battery absorbs the excess current to charge itself, as seen in Figure 14.

5. Comparison Analysis with Different Controllers

To analyze the performance quality of the proposed FF-DISMC controller, the transient and steady-state responses of system were observed with different controllers in terms of time-domain specifications (rise time, percentage undershoot, and settling time).

To examine the converter with PI controller (voltage mode control), the duty cycle to output voltage transfer function is derived from small-signal analysis around the steady-state operating point. It is observed that the unity feedback closed-loop system with that transfer function is unstable. Hence, a PI controller $G_{vm}(s)$ is designed. To tune the parameters of the PI controller, the stability boundary locus method [36] is used with a specified phase margin of 60°.

$$G_{vm}(s) = 6.93795 + \frac{300.33}{s}. \tag{42}$$

To analyze the BQZSDC with dual-loop PI controller (current mode controller), the two essential transfer functions, i.e., duty cycle to the inductor current (i_{L1}) and duty cycle to the output voltage (v_0), are required. The BQZSDC's actual output voltage in the outer loop is compared to the reference DC link voltage, and the voltage error is sent to a voltage loop PI controller. The voltage loop PI generates a reference current signal for the inner loop. The current error is given to the current loop PI controller after comparing the reference current to the actual inductor current. This current PI controller regulates the duty cycle. The controllers are tuned in such a way that the bandwidth of the current control loop is greater than the outer voltage control loop bandwidth. As a result, the dynamics of the current loop are quicker than the outer voltage loop.

Because of unity feedback, the inner loop transfer function was observed as unstable. A PI controller was developed. The PI controller's parameter is tuned using the stability boundary locus approach. The PI controller $G_c(s)$ is as follows:

$$G_c(s) = 0.23795 + \frac{850.33}{s}. \tag{43}$$

To design the outer loop voltage PI controller, the voltage to current transfer function was derived from the analysis. This transfer function's frequency response exhibits a constant gain in the low-frequency range, resulting in a substantial steady-state inaccuracy. A PI controller is designed to eliminate the steady-state error. The PI controller $G_v(s)$ is as follows:

$$G_v(s) = 0.02371 + \frac{36.79}{s}. \tag{44}$$

The DISMC results were also compared to the basic integral SMC (ISMC); the number of control variables used in the ISMC and DISMC equations is the main difference. Only three control variables, x_1, x_2, and x_3, are used in ISMC. The sliding surface equation in ISMC is as follows:

$$S = \alpha_1 x_1 + \alpha_2 x_2 + \alpha_3 x_3, \tag{45}$$

where the control variables are as follows:

$$\begin{aligned} x_1 &= i_{L_1}, \\ x_2 &= v_0, \\ x_3 &= \int (v_0^* - v_0)\mathrm{d}t. \end{aligned} \tag{46}$$

The equivalent control signal of ISMC control input obtained after analysis is as follows:

$$u_{eq} = \frac{-\left(k_1\left(v_b - v_{C_1}\right) + k_2\left(\left(-v_0/R_L\right) + i_{L_2} - (1/r)\left(v_0 - v_{C_1} - v_{C_2}\right) - \left(v_0^* - v_0\right)\right)\right)}{k_1 v_{C_1} + k_2\left(-i_{L_2} + (1/r)\left(v_0 - v_{C_1} - v_{C_2}\right)\right)}. \tag{47}$$

The equivalent controller comprises a control signal $v_C$and a ramp signal v_{ramp}.

$$\begin{aligned} v_C &= -\left(k_1\left(v_b - v_{C_1}\right) + k_2\left(\frac{-v_0}{R_L} + i_{L_2} - \frac{1}{r}\left(v_0 - v_{C_1} - v_{C_2}\right) - \left(v_0^* - v_0\right)\right)\right), \\ v_{\text{ramp}} &= k_1 v_{C_1} + k_2\left(-i_{L_2} + \frac{1}{r}\left(v_0 - v_{C_1} - v_{C_2}\right)\right). \end{aligned} \tag{48}$$

By considering all sliding mode conditions, the performances of the converter with all mentioned controllers with load change in both boost and buck mode are analyzed in Figures 15 and 16.

Tables 2 and 3 examine the transient response of BQZSDC with different controllers in boost and buck modes in terms of time-domain specifications.

6. Conclusion

In this work, an effective control (FF-DISMC) approach has been implemented for BQZSDC. In both buck and boost modes, energy management was achieved between PV, battery, and load. The controller was examined in depth, and its performance was analyzed in both charge (buck) and discharge (boost) modes. The controller met the voltage regulation and battery current regulatory requirements. The proposed controller's performance was also compared to that of other controllers, such as voltage mode, current mode, and single integral SMC, in terms of time-domain specifications such as rise, settling, and percentage peak overshoot. Further, the experimental validation of the proposed control technique on BQZSDC was implemented in both boost and buck modes of operation.

Symbols

i_{L1}:	Current of inductor L_1
i_{L2}:	Current of inductor L_2
i_{Load}:	Load current
i_{C1}:	Current of capacitor C_1
i_{C2}:	Current of capacitor C_2
i_{C0}:	Current of capacitor C_0
i_0:	Converter output current
$I_{L1\text{ref}}$:	Reference current of L_1
v_{C1}:	Voltage of capacitor C_1
v_{C2}:	Voltage of capacitor C_2
v_0:	Voltage of output capacitor C_0 (load voltage)
V_b:	Voltage of battery
V_{ref}:	Reference load voltage
u:	Control input
u_{eq}:	Controller equivalent control input
R_0:	Load resistance
r:	ESR of capacitor C_2
x_1, x_2, x_3, x_4:	Sliding variables
S_1, S_2, S_3:	Switching devices
S:	Sliding surface
α_1, α_2, α_3, α_4:	Sliding coefficients
k_1, k_2, k_3:	Controller gain constants
K:	Reference current gain
p_1, p_2, p_3, p_4, p_5, p_6, p_7:	Coefficients of characteristic equation.

Data Availability

The data (converter parameters) used to support the findings of this study are included in the article.

Conflicts of Interest

The authors declare that they have no conflicts of interest.

References

[1] T. Tasi-Fu Wu, S. Yu-Kai Chen, and Y. Chen, "Modeling PWM DC/DC converters out of basic converter units," *IEEE Transactions on Power Electronics*, vol. 13, no. 5, pp. 870–881, 1998.

[2] D. Bao, A. Kumar, X. Pan, X. Xiong, A. R. Beig, and S. K. Singh, "Switched inductor double switch high gain DC-DC converter for renewable applications," *IEEE Access*, vol. 9, pp. 14259–14270, 2021.

[3] Q. Qun Zhao and F. C. Lee, "High-efficiency, high step-up dc-dc converters," *IEEE Transactions on Power Electronics*, vol. 18, no. 1, pp. 65–73, 2003.

[4] F. Z. Fang Zheng Peng, "*Z*-source inverter," *IEEE Transactions on Industry Applications*, vol. 39, no. 2, pp. 504–510, 2003.

[5] J. Abbasi Bolaghi, A. Taheri, and M. H. Babaei, "Switched-capacitor inductor *Z*-source inverter with an impedance network," *International Transactions on Electrical Energy Systems*, vol. 31, no. 5, 2021.

[6] M. Mohammadi, A. Mirzaee, J. S. Moghani, J. Milimonfared, and M. Zarei Tazehkand, "A quasi-*Z*-source inverter with

a single high-frequency-switch," *International Transactions on Electrical Energy Systems*, vol. 31, no. 3, pp. 1–18, 2021.

[7] M. Hanif, M. Basu, and K. Gaughan, "Understanding the operation of a *Z*-source inverter for photovoltaic application with a design example," *IET Power Electronics*, vol. 4, no. 3, p. 278, 2011.

[8] J. Liu, S. Jiang, D. Cao, and F. Z. Peng, "A digital current control of quasi-*Z*-source inverter with battery," *IEEE Transactions on Industrial Informatics*, vol. 9, no. 2, pp. 928–937, 2013.

[9] D. Vinnikov and I. Roasto, "Quasi-*Z*-source-based isolated DC/DC converters for distributed power generation," *IEEE Transactions on Industrial Electronics*, vol. 58, no. 1, pp. 192–201, 2011.

[10] J. Liu, J. Wu, J. Qiu, and J. Zeng, "Switched *Z*-source/quasi-*Z*-source DC-DC converters with reduced passive components for photovoltaic systems," *IEEE Access*, vol. 7, pp. 40893–40903, 2019.

[11] F. L. Luo and H. Ye, "Small signal analysis of energy factor and mathematical modeling for power dc-dc converters," *IEEE Transactions on Power Electronics*, vol. 22, no. 1, pp. 69–79, 2007.

[12] Y. Zhang, Q. Liu, J. Li, and M. Sumner, "A common ground switched-quasi-Z-source bidirectional DC-DC converter with wide-voltage-gain range for EVs with hybrid energy sources," *IEEE Transactions on Industrial Electronics*, vol. 65, no. 6, pp. 5188–5200, 2018.

[13] V. V. S. K. Bhajana, P. Drabek, and P. K. Aylapogu, "Design and implementation of a zero voltage transition bidirectional DC-DC converter for DC traction vehicles," *International Transactions on Electrical Energy Systems*, vol. 29, no. 5, Article ID e2842, 2019.

[14] Y. Raj Kafle, M. J. Hossain, and M. Kashif, "Quasi-*Z*-source -based bidirectional DC-DC converters for renewable energy applications," *International Transactions on Electrical Energy Systems*, vol. 31, no. 4, pp. 1–16, 2021.

[15] S. S. Somalinga and K. R. Santha, "Non-isolated enhanced gain of DC-DC converter for DC micro-grid applications," *International Transactions on Electrical Energy Systems*, vol. 30, no. 12, pp. 1–20, 2020.

[16] S. Battula, M. M. Garg, A. Kumar Panda, M. Preetam Korukonda, and L. Behera, "Analysis and dual-loop PI control of bidirectional quasi *Z*-source DC-DC converter," in *Proceedings of the IECON 2020—46th Annual Conference of the IEEE Industrial Electronics Society*, Singapore, October 2020.

[17] A. Hussain, M. M. Garg, M. P. Korukonda, S. Hasan, and L. Behera, "A parameter estimation based MPPT method for a PV system using lyapunov control scheme," *IEEE Transactions on Sustainable Energy*, vol. 10, no. 4, pp. 2123–2132, 2019.

[18] Y. Tang, D. Fu, T. Wang, Z. Xu, and Z. Xu, "Hybrid switched-inductor converters for high step-up conversion," *IEEE Transactions on Industrial Electronics*, vol. 62, no. 3, pp. 1480–1490, 2015.

[19] Y. Tang, T. Wang, and Y. He, "A Switched-capacitor-based active-network converter with high voltage gain," *IEEE Transactions on Power Electronics*, vol. 29, no. 6, pp. 2959–2968, 2014.

[20] Y.-S. Lee and Y.-P. Ko, "Switched-capacitor bi-directional converter performance comparison with and without quasi-resonant zero-current switching," *IET Power Electronics*, vol. 3, no. 2, p. 269, 2010.

[21] O. Cornea, G.-D. Andreescu, N. Muntean, and D. Hulea, "Bidirectional power flow control in a DC microgrid through a switched-capacitor cell hybrid DC-DC converter," *IEEE Transactions on Industrial Electronics*, vol. 64, no. 4, pp. 3012–3022, 2017.

[22] Y. Zhang, C. Fu, M. Sumner, and P. Wang, "A wide input-voltage range quasi-*Z*-source boost DC-DC converter with high-voltage gain for fuel cell vehicles," *IEEE Transactions on Industrial Electronics*, vol. 65, no. 6, pp. 5201–5212, 2018.

[23] A. Özdemir and Z. Erdem, "Double-loop PI controller design of the DC-DC boost converter with a proposed approach for calculation of the controller parameters," *Proceedings of the Institution of Mechanical Engineers—Part I: Journal of Systems & Control Engineering*, vol. 232, no. 2, pp. 137–148, 2018.

[24] W. Rui, S. Qiuye, Z. Pinjia, G. Yonghao, Q. Dehao, and W. Peng, "Reduced-order transfer function model of the droop-controlled inverter via Jordan continued-fraction expansion," *IEEE Transactions on Energy Conversion*, vol. 35, no. 3, pp. 1585–1595, 2020.

[25] R. Wang, Q. Sun, P. Tu, J. Xiao, Y. Gui, and P. Wang, "Reduced-order aggregate model for large-scale converters with inhomogeneous initial conditions in DC microgrids," *IEEE Transactions on Energy Conversion*, vol. 36, no. 3, pp. 2473–2484, 2021.

[26] P. Padmavathi and S. Natarajan, "Single switch quasi *Z*-source based high voltage gain DC-DC converter," *International Transactions on Electrical Energy Systems*, vol. 30, no. 7, pp. 1–25, 2020.

[27] H. Komurcugil, "Sliding mode control strategy with maximized existence region for DC-DC buck converters," *International Transactions on Electrical Energy Systems*, vol. 31, no. 3, pp. 1–14, 2021.

[28] B. Wang, J. Xu, R.-J. Wai, and B. Cao, "Adaptive sliding-mode with hysteresis control strategy for simple multimode hybrid energy storage system in electric vehicles," *IEEE Transactions on Industrial Electronics*, vol. 64, no. 2, pp. 1404–1414, 2017.

[29] S. Oucheriah, L. Guo, and S. Member, "PWM-based adaptive sliding-mode control for boost DC-DC converters," *IEEE Transactions on Industrial Electronics*, vol. 60, no. 8, pp. 3291–3294, 2013.

[30] M. A. Qureshi, I. Ahmad, and M. F. Munir, "Double integral sliding mode control of continuous gain four quadrant quasi-*Z*-source converter," *IEEE Access*, vol. 6, pp. 77785–77795, 2018.

[31] A. F. Ayad and R. M. Kennel, "Model predictive controller for grid-connected photovoltaic based on quasi-*Z*-source inverter," in *Proceedings of the 2013 IEEE International Symposium on Sensorless Control for Electrical Drives and Predictive Control of Electrical Drives and Power Electronics (SLED/PRECEDE)*, pp. 3–8, Munich, Germany, October 2013.

[32] D. Ma, X. Cao, C. Sun et al., "Dual-predictive control with adaptive error correction strategy for AC microgrids," *IEEE Transactions on Power Delivery*, vol. 37, pp. 1–11, 2021.

[33] Q. Sun, R. Han, H. Zhang, J. Zhou, and J. M. Guerrero, "A multiagent-based consensus algorithm for distributed

coordinated control of distributed generators in the energy internet," *IEEE Transactions on Smart Grid*, vol. 6, no. 6, pp. 3006–3019, 2015.

[34] S. C. Siew-Chong Tan, Y. M. Lai, and C. K. Tse, "Indirect sliding mode control of power converters via double integral sliding surface," *IEEE Transactions on Power Electronics*, vol. 23, no. 2, pp. 600–611, 2008.

[35] H. Komurcugil, S. Biricik, and N. Guler, "Indirect sliding mode control for DC-DC SEPIC converters," *IEEE Transactions on Industrial Informatics*, vol. 16, no. 6, pp. 4099–4108, 2020.

[36] M. M. Garg, Y. V. Hote, M. K. Pathak, and L. Behera, "An approach for buck converter PI controller design using stability boundary locus," in *Proceedings of the IEEE PES T & D Conference and Exposition*, Denver, CO, USA, April 2018.